applied sciences

MDPI

Article

Research on a New Electromagnetic Ultrasonic Pipeline Unidirectional Wave Defect Imaging Method

Longlong He and Yunlai Zhou *

School of Aerospace Engineering, Xi'an Jiaotong University, Xi'an 710049, China
* Correspondence: yunlaizhou@xjtu.edu.cn

Abstract

Pipeline inspection has long been a major research topic in non-destructive testing (NDT). Conventional electromagnetic acoustic transducers (EMATs) generally generate bidirectional ultrasonic waves, which exhibit several inherent limitations in defect detection, including low signal amplitude, limited directivity, and incompatibility with pulse-echo inspection configurations. The use of unidirectional guided waves generated by EMATs offers a potential means of addressing these limitations in pipeline inspection. In this study, a method for pipeline defect imaging using electromagnetic ultrasonic unidirectional waves is investigated. First, the generation mechanism of unidirectional waves is theoretically analyzed based on the principle of wave superposition. Subsequently, finite element simulations are performed to investigate the effects of key transducer parameters on the amplitude of the generated unidirectional waves, and an optimal combination of excitation parameters is determined. Finally, defect imaging experiments are conducted on pipelines containing different types of defects. The simulation and experimental results show that the signal amplitude of the electromagnetic ultrasonic unidirectional waves increases by approximately 57.3% after optimization using an orthogonal experimental design. Experimental B-scan results show that the proposed bidirectional B-scan synthesis method provides a qualitative visualization and profile assessment of the defects.

Keywords: EMAT; unidirectional wave; pipeline inspection; defect imaging

1. Introduction

Electromagnetic acoustic transducers (EMATs) are a non-destructive testing (NDT) technology well suited to industrial applications in which contact-based inspection is impractical. Unlike conventional piezoelectric transducers, EMATs generate ultrasound directly within electrically conductive materials without requiring a couplant [1,2]. Their non-contact operation, tolerance of harsh environments, and applicability to both ferromagnetic and non-ferromagnetic materials make them attractive for long-range guided-wave inspection of pipelines, where access may be limited and operating conditions can be demanding [3–5]. Over the past decade, research has focused on improving EMAT energy-conversion efficiency, mode selectivity, flexibility, and unidirectional wave generation [6,7].

EMATs have been extensively investigated for generating several ultrasonic wave modes, including shear-horizontal (SH), Lamb, and Rayleigh waves. Miao and Li [8]

Academic Editor: Alexander Sutin

Received: 2 September 2026
Revised: 23 October 2026
Accepted: 27 October 2026
Published: 4 November 2026

Copyright: © 2026 by the authors. Licensee MDPI, Basel, Switzerland. This article is an open access article distributed under the terms and conditions of the Creative Commons Attribution (CC BY) license.

reviewed SH-wave transducers and classified them into Lorentz-force-based EMATs, magnetostrictive transducers, and piezoelectric wedge transducers. They highlighted the nondispersive characteristics of the fundamental SH0 mode, which are beneficial for long-range inspection. To address the low energy-conversion efficiency of conventional EMATs, researchers have proposed optimized configurations. Sun et al. [9] developed an oblique point-focusing SH guided-wave EMAT and established analytical models for selecting the focal position, reporting enhanced signal amplitudes. Huang et al. [10] designed a point-focusing EMAT for T(0,1) guided waves in pipelines and reported an approximately 60% increase in defect-reflection intensity. Flexibility is another important development. Liu et al. [11] introduced a flexible, coil-only EMAT that uses a planar magnetic coil driven by a rectangular pulsed current to generate a quasi-static magnetic field, thereby eliminating permanent magnets. This design can conform to curved surfaces and may simplify inspection of complex structures.

Pipeline inspection is a major application area for EMATs. Guided waves can travel relatively long distances, making them useful for detecting cracks, corrosion, and wall-thickness loss in ferromagnetic and non-ferromagnetic pipelines [2,12]. Selecting an appropriate guided-wave mode is essential. Torsional modes, particularly T(0,1), are widely used because of their nondispersive behavior and sensitivity to certain axial defects. Liu et al. [13] developed a plug-in magnetostrictive transducer for ferromagnetic pipelines and optimized the circumferential static magnetic field to increase signal amplitude. Deng et al. [14] used T(0,1) waves to measure axial stress in hollow steel cylinders and proposed an LMS–Gabor algorithm for extracting small time shifts. Longitudinal modes, such as L(0,2), can be used to detect circumferential defects. Xie et al. [15] designed a plug-in EMAT with periodically pulsed electromagnets for non-ferromagnetic pipelines and reported a higher signal amplitude than that obtained with a conventional permanent-magnet design. Liu et al. [16] used leaky L(0,2) waves to measure phase interfaces in liquid-filled pipelines.

A range of studies has demonstrated the use of EMATs for detecting defects in pipelines. Wang et al. [17] improved periodic-permanent-magnet (PPM) EMATs for inspecting 90° aluminum-alloy pipeline bends and identified defects at the intrados, sides, and extrados, with reported cross-sectional area losses as low as 0.48%. Hu et al. [18] used CSH0 waves to detect defects behind support structures and reported the detection of 3 mm cracks after the waves passed through welded supports. For buried or liquid-filled pipelines, Liu et al. [19] combined T(0,1) guided waves with 11-bit Barker-code encoding and reported a defect-location error below 1%. Thon et al. [20] used a linear-array EMAT and reflected higher-order SH modes for remote thickness gauging, estimating the minimum thickness with a maximum error of 0.4 mm over a propagation distance of 600 mm. EMATs are also useful in high-temperature environments where conventional couplants may be unsuitable. Zhou et al. [21] developed a water-cooled EMAT for pipelines at temperatures up to 630 °C and reported detection of 3 mm holes after 10 min of continuous operation. The transducer was designed to adapt to pipeline curvature, improving contact-free inspection under demanding conditions.

Despite substantial progress in EMAT-based pipeline inspection, systematic studies of parameter optimization for unidirectional-wave excitation and its application to different defect types remain limited. This study therefore investigates electromagnetic-acoustic unidirectional guided waves for pipeline defect detection through numerical simulation and experiments. The work comprises three stages. First, the generation mechanism of unidirectional waves is analyzed using the principle of superposition. Second, finite-element simulations are used to evaluate how key transducer parameters affect wave amplitude, and an optimal parameter combination is identified using an orthogonal experimental design. Third, an EMAT probe and an aluminum pipeline

specimen containing multiple defects are fabricated based on the simulation results. An experimental platform is then assembled, and imaging tests are conducted to assess the method for different defect types.

2. Theoretical Basis

When two or more sources generate waves in the same specimen, the resulting ultrasonic field can be described by the principle of superposition. Each conductor in a meander-line EMAT coil can be treated, in a simplified model, as a localized source. When waves of the same frequency and vibration direction meet with a fixed phase difference, their displacements may interfere constructively at some locations and destructively at others; under suitable conditions, the resultant displacement may approach zero.

The waveform of an ultrasonic wave generated by an EMAT can be expressed as follows:

$$y=u\cos\left[\omega\left(t-\frac{x}{v}\right)+\varphi\right] \quad (1)$$

Here, x denotes the equilibrium position; y is the displacement of a particle from its equilibrium position along the X-axis; u is the particle-displacement vector; $\omega = 2\pi/T$; T is the period; t is time; v is the wave speed; and φ is the phase.

For EMATs A and B (Figure 1), assuming zero initial phase and the same frequency, the displacement of the resultant wave can be expressed as follows:

$$y=u_A\cos\left[\omega\left(-t-\frac{x}{v}\right)\right]+u_B\cos\left[\omega\left(-t-\Delta t-\frac{x+\Delta x}{v}\right)\right] \quad (2)$$

Here, y_A and y_B denote the particle displacements generated by EMATs A and B, respectively; u_A and u_B are their corresponding particle-displacement vectors; Δt is the delay of the excitation current in EMAT B relative to that in EMAT A; and Δx is the distance between EMATs A and B.

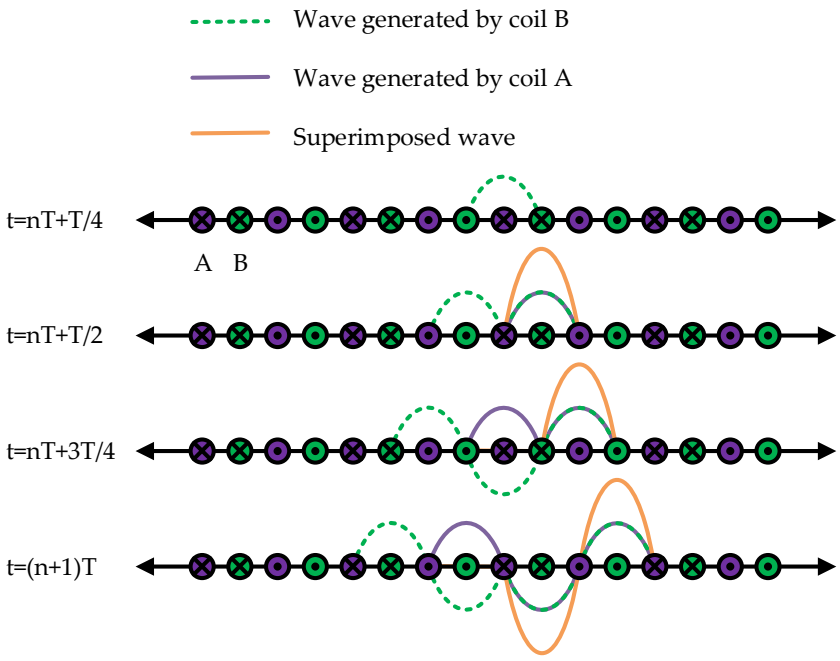


Figure 1. The excitation principle of EMAT unidirectional wave.

For the left-propagating component to cancel after superposition, the two contributions must have equal displacement amplitudes ($u_A = u_B$) and a phase difference of (2n + 1)T/2, where n is an integer. To minimize the spacing between EMATs A and B

and reduce the influence of multiple cycles, the phase difference is set to T/2. The expression can then be simplified as follows:

$$\omega\left(-t-\Delta t-\frac{x+\Delta x}{v}\right)-\omega\left(-t-\frac{x}{v}\right)=\omega\times\frac{T}{2} \tag{3}$$

Rearranging Equation (3) gives

$$\Delta x=\frac{\lambda}{4} \tag{4}$$

$$\Delta t=\frac{T}{4} \tag{5}$$

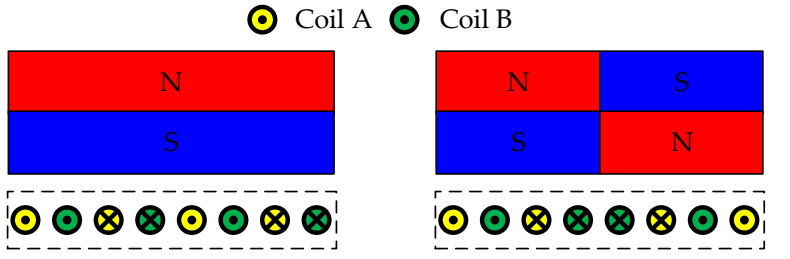
Here, λ denotes the wavelength. The expressions indicate that, when the spacing between adjacent wires of EMATs A and B is $\lambda/4$ and the excitation current in EMAT B is delayed by T/4 relative to that in EMAT A, the left-propagating components cancel. Because each EMAT generates waves in both directions, the corresponding delay relationship for rightward propagation is

$$\omega\left(t-\Delta t-\frac{x-\Delta x}{v}\right)-\omega\left(t-\frac{x}{v}\right)=0 \tag{6}$$

Substituting Equations (4) and (5) into Equation (6) yields zero for the relevant phase difference; thus, the two waves propagate in phase toward the right, and their resultant amplitude is the sum of their individual amplitudes.

Figure 1 illustrates the operating principle of the EMAT-based unidirectional-wave excitation method. High-frequency pulse currents of the same frequency and amplitude, with a phase difference of 90°, are applied to coils A and B. The coil spacing is $\lambda/4$, where λ is the ultrasonic wavelength. At t = nT, the particle beneath coil B begins to generate an ultrasonic wave. At t = nT + T/4, the particle beneath coil A begins to generate a wave, while the wave generated by coil B has traveled a distance of $\lambda/4$. On the right side of the coil center, the waves generated by coils A and B are in phase, and their displacements add constructively; the resultant displacement is twice that generated by either coil alone. This is the enhanced-propagation side. On the left side, the waves are out of phase and cancel ideally, forming the suppressed-propagation side.

The conventional EMAT structure used to generate unidirectional waves in plates is shown in Figure 2a. It consists of a permanent magnet and two coils. According to Equation (4) and (5), the coil spacing is one-quarter of the wavelength, and the excitation delay is one-quarter of the period. For pipeline inspection, this study proposes the EMAT structure shown in Figure 2b. The permanent-magnet assembly comprises two magnets with opposite poles, and the excitation coil is arranged symmetrically. The coil spacing and excitation delay are retained from the conventional configuration.



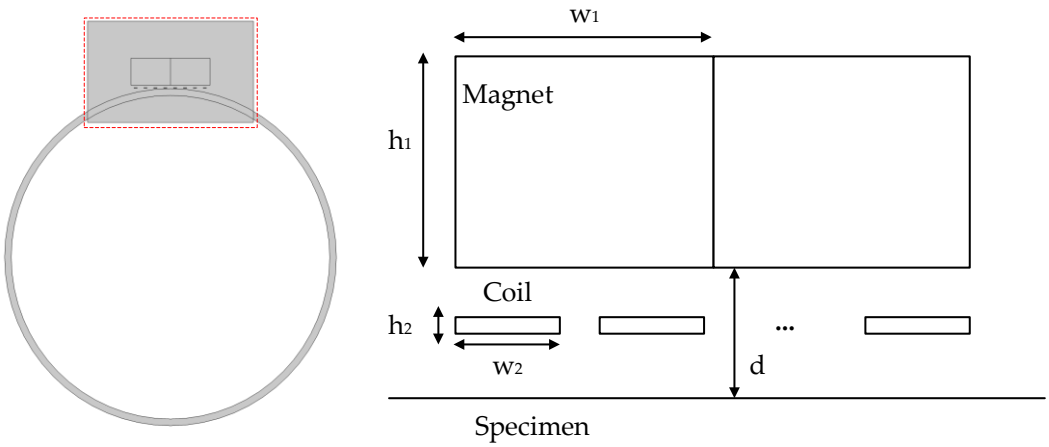
(**a**) Traditional plate structure (**b**) New pipeline structure

Figure 2. Structure of EMAT for plates and pipelines.

3. Simulation

3.1. Simulation Model

A two-dimensional finite-element model of EMAT-based unidirectional-wave pipeline inspection was developed in COMSOL Multiphysics 6.0, as shown in Figure 3a. The model consists primarily of an aluminum pipeline, an EMAT module, and an air domain. The pipeline has an inner diameter of 96 mm and an outer diameter of 100 mm. The air domain is a 50 mm × 30 mm rectangular region. The EMAT module comprises a permanent magnet and an excitation coil. The magnet is made of NdFeB and consists of two rectangular magnets, each measuring 12 mm × 8 mm. The meander-line excitation coil is divided into two groups, each containing four conductors. Each conductor is 1.0 mm wide and 0.1 mm thick, and the lift-off distance is 0.1 mm. The spacing between adjacent conductors is 2.98 mm. The excitation frequency is 434 kHz, selected for the circumferential guided-wave mode "Clamb0" (corresponding to the A0 mode in a flat plate).



(**a**) Simulation model (**b**) EMAT Parameters

Figure 3. Simulation model and EMAT Parameters for unidirectional wave pipeline inspection.

The phase-velocity dispersion curves of a hollow aluminum pipeline with a wall thickness of 2 mm and an outer diameter of 100 mm are shown in Figure 4. As shown in the figure, at an excitation frequency of 434 kHz, only two guided-wave modes, Clamb0 and Clamb1, are excited in the pipeline. The phase velocities of the Clamb0 and Clamb1 modes are 2980 m/s and 5170 m/s, respectively, indicating a substantial difference between the two modes. In this study, the principle of coherent synthesis of the meander-line coil is employed in reverse to suppress the undesired Clamb1 mode. Specifically, the spacing between adjacent coils is set to one-quarter of the wavelength corresponding to the Clamb1 mode. Under this configuration, the Clamb1 mode is expected to undergo destructive interference and is therefore significantly suppressed. Although the amplitude of the Clamb0 mode does not reach its maximum under this configuration, the suppression of the Clamb1 mode improves the modal purity of the generated wave packet and consequently facilitates a cleaner time-domain waveform.

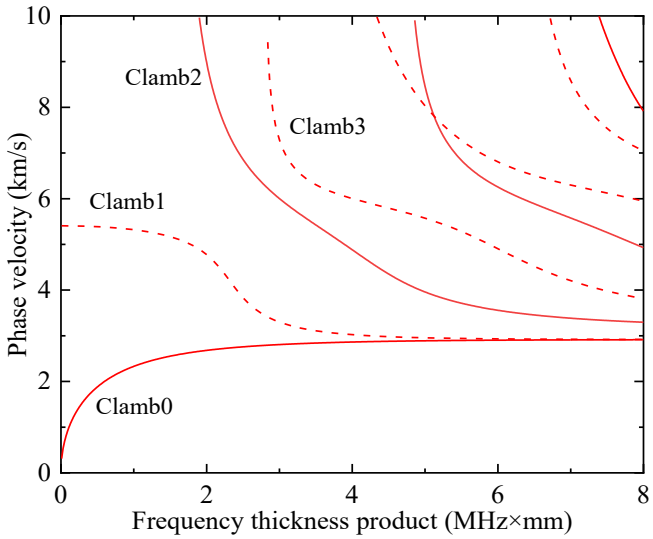


Figure 4. Dispersion curve of 2 mm thick and 100 mm diameter hollow aluminum pipeline.

The time step was set to T/20, where T is the excitation period, and the total simulation time was 200 T, which was intended to capture defect-reflected wave signals. The generalized-α method was used as the solver. The coil currents were sinusoidally modulated tone-burst signals, with a phase delay of one-quarter of a period between the two coils, as shown in Figure 5. Each excitation signal contained five cycles at the fundamental frequency. The peak excitation current was I_{max} = 10 A. The expressions for the two current signals are provided in Table 1.

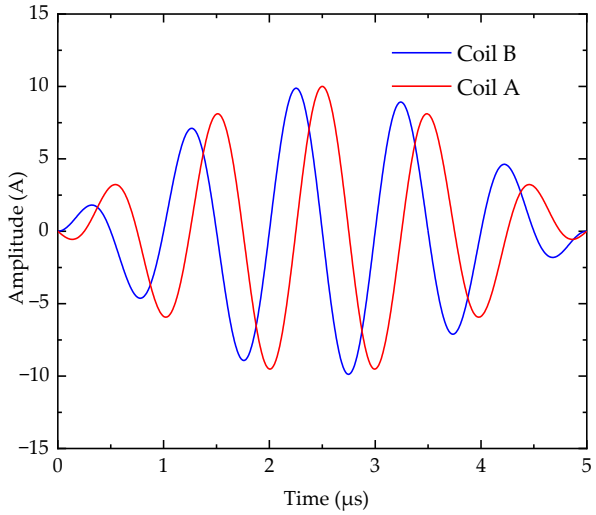


Figure 5. The excitation signals of the two coils.

Table 1. The expressions of the two excitation current signals.

Coil	Excitation Current Expression	Time
CoilA	sin(2 × π×f × t) × sin(2 × π×f × t/10) × 10[A]	(0, 5)T
CoilB	sin(2 × π×f × t-π/2) × sin(2 × π×f × t/10) × 10[A]	(0, 5)T

3.2. Orthogonal Experimental Design Optimization

The parameters expected to affect the amplitude of the unidirectional excitation signal in EMAT-based pipeline inspection include the permanent-magnet and excitation-coil parameters shown in Figure 3b (schematic and not to scale). The magnet parameters are width w_1 and thickness h_1; the coil parameters are width w_2, thickness h_2, and lift-off

distance d. The parameter ranges were selected based on common EMAT specifications for aluminum-plate inspection, manufacturing constraints, and the capabilities of the current driving circuit, as summarized in Table 2. Because the five parameters may interact, a full factorial study with four levels per parameter would require $4^5 = 1024$ simulations, imposing a substantial computational burden.

Table 2. The value levels of the five parameters to be optimized.

Parameters	Magnet Width w_1 (mm)	Magnet Thickness h_1 (mm)	Coil Width w_2 (mm)	Coil Thickness h_2 (mm)	Lift-off Distance d (mm)
Level 1	10	6	0.5	0.1	0.1
Level 2	12	8	1	0.2	0.2
Level 3	14	10	1.5	0.3	0.3
Level 4	16	12	2	0.4	0.4

To identify a parameter combination that maximizes the unidirectional-wave amplitude and to characterize the individual effects of the parameters, an orthogonal experimental design was used. Orthogonal design is a fractional-factorial approach that can reduce the number of simulations required. For five factors at four levels each, a full factorial design requires 1024 runs, whereas the L16 (4^5) orthogonal array requires 16 runs. The tested combinations and corresponding signal amplitudes are listed in Table 3.

Table 3. The value combinations and signal amplitudes of the five-parameter four-level orthogonal test.

Number	Parameter 1 (w_1)	Parameter 2 (h_1)	Parameter 3 (w_2)	Parameter 4 (h_2)	Parameter 5 (d)	Amplitude ($\times 10^{-8}$ mm)
1	1	1	1	1	1	60.1
2	1	2	2	2	2	85.5
3	1	3	3	3	3	42.7
4	1	4	4	4	4	52.5
5	2	1	2	3	4	45.6
6	2	2	1	4	3	52.4
7	2	3	4	1	2	72.4
8	2	4	3	2	1	91.1
9	3	1	3	4	2	64.7
10	3	2	4	3	1	89.9
11	3	3	1	2	4	71.1
12	3	4	2	1	3	55.6
13	4	1	4	2	3	80.8
14	4	2	3	1	4	58.7
15	4	3	2	4	1	46.9

16	4	4	1	3	2	29.2

Following the principle of comparability in orthogonal experimental design, the mean signal amplitude at each level of each parameter was calculated (denoted by k_i, where i is the level index). The level-wise means and range values are presented in Figure 6 and Table 4. The results indicate that the unidirectional-wave amplitude decreases as lift-off distance increases, increases gradually with coil width, and first increases and then decreases as magnet width, magnet thickness, and coil thickness increase.

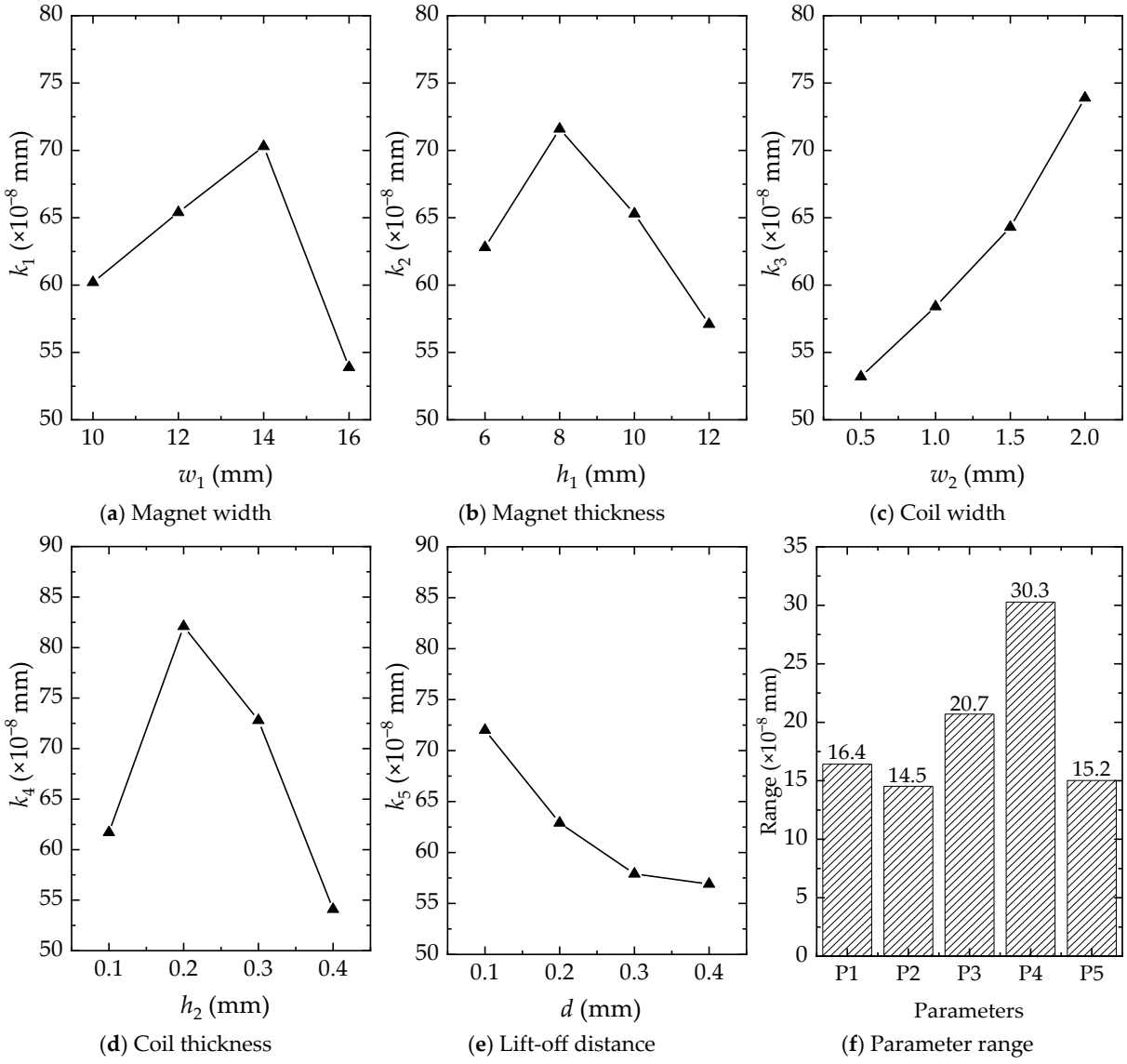


Figure 6. Influence of each parameter on the unidirectional wave amplitude and parameter range.

Table 4. Analysis results of the five-parameter four-level orthogonal experiment.

Levels	Parameter 1 (w_1)	Parameter 2 (h_1)	Parameter 3 (w_2)	Parameter 4 (h_2)	Parameter 5 (d)
Level 1	60.2	62.8	53.2	61.7	72.0
Level 2	65.4	71.6	58.4	82.1	62.9
Level 3	70.3	58.3	64.3	51.8	57.9

Level 4	53.9	57.1	73.9	54.1	56.9
Range	16.4	14.5	20.7	30.3	15.2

The range analysis suggests that coil width w_2 and coil thickness h_2 have greater effects on the signal amplitude than magnet width w_1, magnet thickness h_1, and lift-off distance d. The orthogonal-design analysis identified 32,421 as the optimal parameter-level combination: magnet width = 14 mm, magnet thickness = 8 mm, coil width = 2 mm, coil thickness = 0.2 mm, and lift-off distance = 0.1 mm. This combination was not included in the L16 array. Before optimization, the simulated amplitude was 79.2 × 10^{-8} mm. The orthogonal analysis predicted an amplitude of 120.2 × 10^{-8} mm for the selected combination; a subsequent finite-element simulation yielded 124.6 × 10^{-8} mm, close to the prediction.

The time-domain waveform comparison of the unidirectional wave signal under the optimal parameter combination and that under the initially adopted excitation parameters in the previous section is shown in Figure 7. It can be seen that after orthogonal experimental optimization, the unidirectional wave signal amplitude is enhanced, with an increase of approximately 57.3%. Figure 8 shows the stress nephograms of the unidirectional wave in the pipeline at different time. It can be observed from the figure that after orthogonal experimental optimization, the displacement amplitude on the right side of the unidirectional wave is higher than that on the left side.

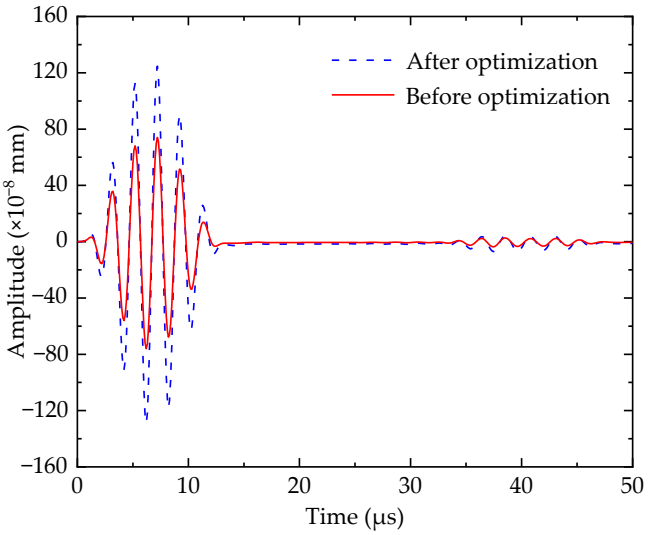


Figure 7. Comparison of unidirectional wave signals before and after optimization.

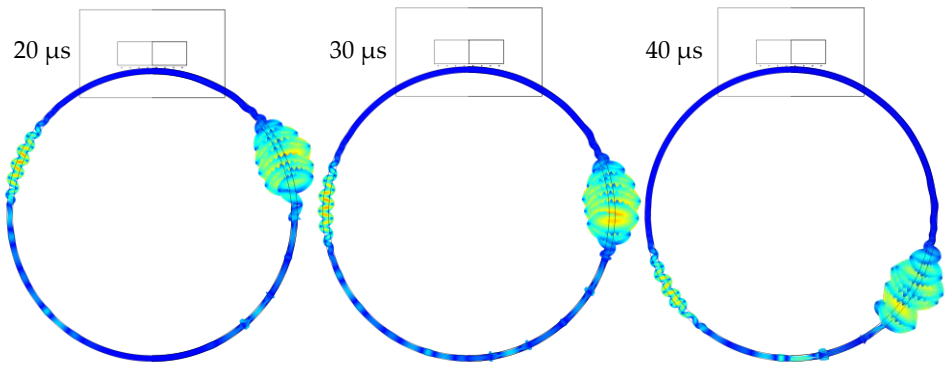
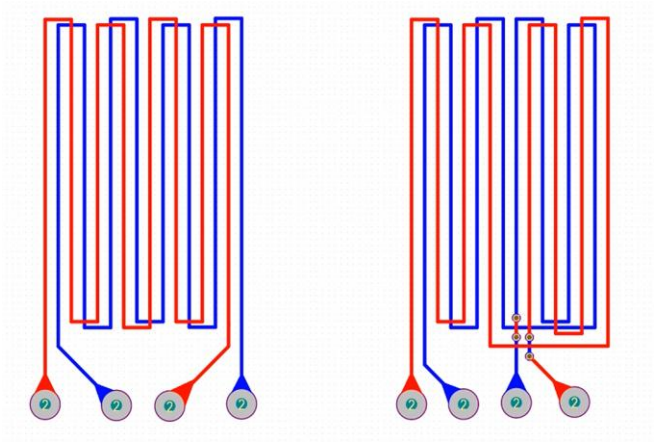


Figure 8. Stress nephograms of the unidirectional wave in the pipeline at different times.

4. Experiments

4.1. Experimental Setup

A coil (Figure 9) was designed to validate the proposed unidirectional-wave excitation method for pipelines. Figure 9a shows the conventional plate-type coil, and Figure 9b shows the proposed pipeline coil. Both were fabricated using printed-circuit-board (PCB) technology and consisted of four turns. Each coil used a five-split design intended to increase the excitation-signal amplitude. The coils were designed in Altium Designer, with a line spacing of 2.98 mm, a split width of 10 mil (1 mil ≈ 0.0254 mm), and a split spacing of 11 mil. These parameters were selected to excite the CLamb0 mode wave at 434 kHz in the 2 mm thick aluminum pipeline.



(**a**) Traditional plate coil (**b**) New pipeline coil

Figure 9. Design of electromagnetic acoustic unidirectional wave coils.

The aluminum pipeline specimen containing the defects had an outer diameter of 100 mm, a wall thickness of 2 mm, and a length of 200 mm. It contained three through-wall defects. A 10 mm diameter circular hole was located 50 mm from the left end face at a circumferential position of 90°. A rectangular groove, 20 mm long and 5 mm wide, was located at the bottom of the specimen (180° circumferential position). A 15 mm diameter circular hole was located 50 mm from the right end face at a circumferential position of 270°. The defect locations are shown in Figure 10.

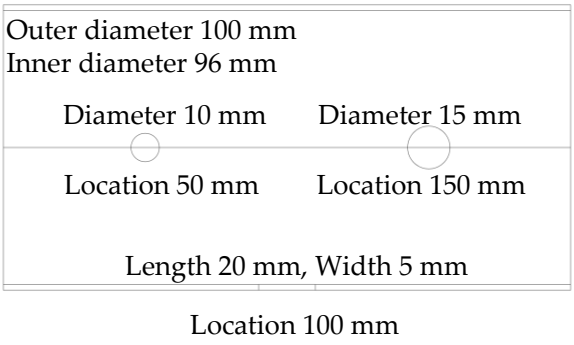


Figure 10. Schematic diagram of the pipeline specimen and defect locations.

Figure 11 shows the experimental platform for EMAT-based unidirectional-wave NDT. The RAM-5000 system served as the main excitation and acquisition unit. During transmission, the system generated a high-energy tone-burst signal that passed through a

high-pass filter, an impedance-matching network, and a diplexer before reaching the transducer. The matching network was used to improve power transfer, while the high-pass filter was intended to remove DC offset and power-line interference. The transducer operated in pulse-echo mode through the diplexer, first exciting the ultrasonic wave and then receiving defect-reflected echoes. The received signal passed through a low-pass filter to attenuate high-frequency noise and was then amplified by a preamplifier before acquisition. The conditioned signal was returned to the RAM-5000 for digitization and processing. A host computer controlled the parameters and stored data, while an oscilloscope monitored the waveform in real time.

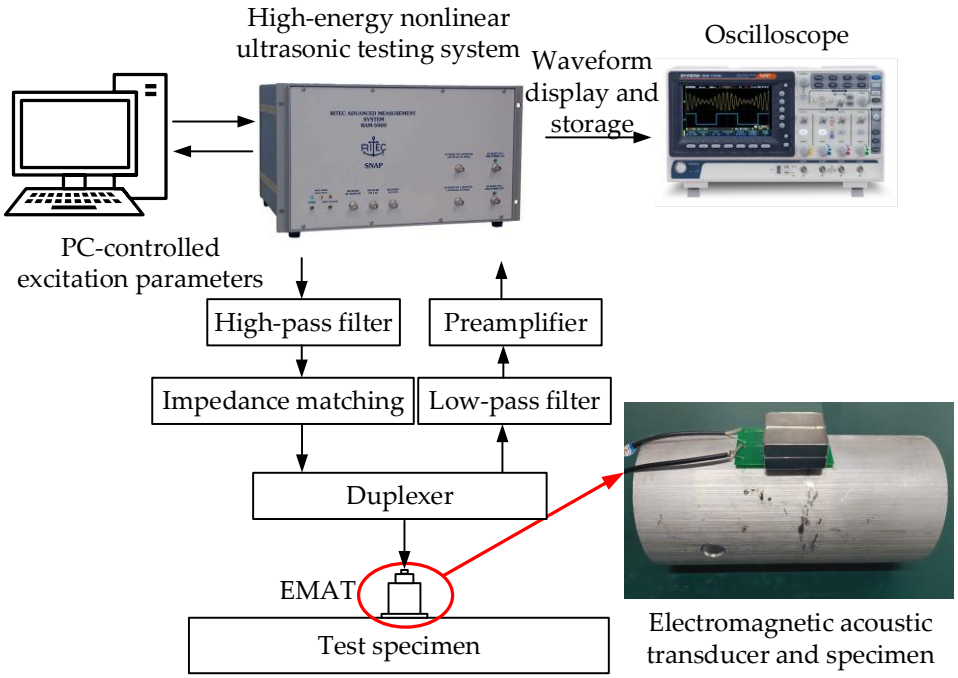


Figure 11. Electromagnetic ultrasonic non-destructive testing experimental platform.

4.2. Results and Analysis

In the experiment, two surface-mounted piezoelectric wafers were bonded to the outer surface of the pipe at symmetric positions on the enhanced side and the suppressed side of the EMAT. The transducer was driven by a five-cycle tone-burst signal at 434 kHz, and the signals from both wafers were recorded simultaneously. Figure 12 compares the time-domain waveforms received on the two sides. The peak amplitude on the enhanced side is 32.6 mV, while that on the suppressed side is 5.1 mV, giving an amplitude ratio of about 6.4:1. This provides direct experimental evidence that the proposed transducer generates predominantly unidirectional wave propagation.

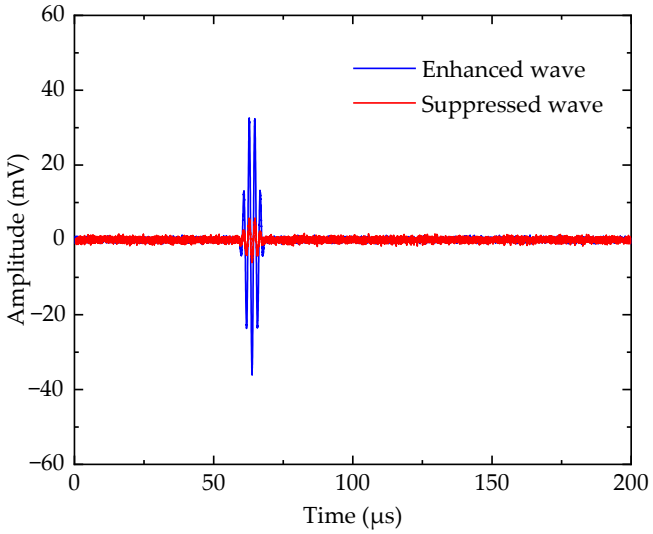
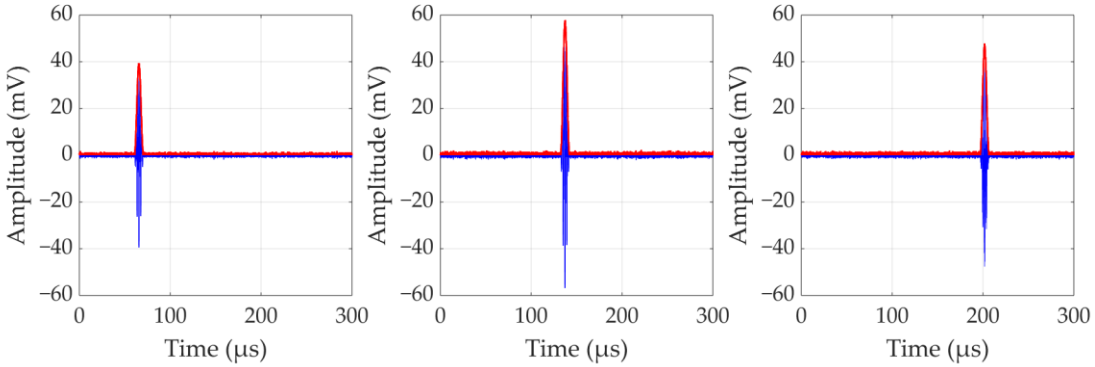


Figure 12. Comparison of the time-domain waveforms of the enhanced wave and the suppressed wave.

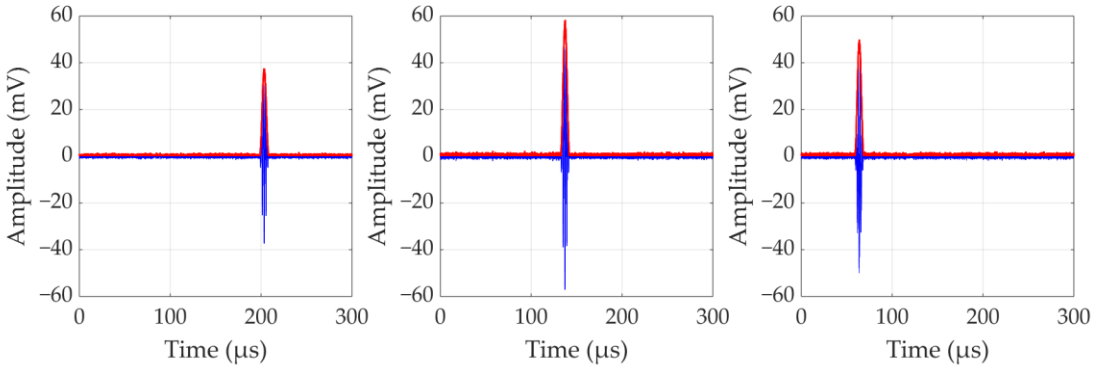
Using the experimental platform described in Section 4.1, defect-imaging tests were performed on a pipeline containing different defect types. A conventional B-scan provides a left-side or right-side view of a defect. The proposed procedure comprises three steps: (1) acquire a left-side B-scan; (2) acquire a right-side B-scan and flip it horizontally; and (3) synthesize the two images by calculating their intersection, implemented here as an element-wise (Hadamard) product. The method is intended to improve defect-shape representation while reducing the influence of signals from the suppressed propagation side.

The B-scan procedure was implemented as follows. During the left-side scan, the phase of coil A led that of coil B by 90°; during the right-side scan, coil A lagged coil B by 90°. The probe operated in a self-transmit/receive configuration and was scanned along the specimen's axial direction in 1 mm increments. In order to reduce the influence of wave packet broadening on the subsequent defect B-scan imaging results, windowing processing was applied to the experimental signal. The window width was 5 periods of the excitation signal, as shown by the red curves in Figures 13 and 14.



(**a**) Transducer position 50 mm (**b**) Transducer position 100 mm (**c**) Transducer position 150 mm

Figure 13. Time-domain waveforms at different positions of the left-side B-scan using unidirectional waves.



(**a**) Transducer position 50 mm (**b**) Transducer position 100 mm (**c**) Transducer position 150 mm

Figure 14. Time-domain waveforms at different positions of the right-side B-scan using unidirectional waves.

The time-domain waveforms acquired at different probe positions during the left- and right-side B-scans are shown in Figures 13 and 14. When the probe was positioned over a defect, the echo amplitude was lowest for the 10 mm diameter circular hole, intermediate for the 15 mm diameter hole, and highest for the 20 mm long rectangular groove. During leftward propagation, the 10 mm hole was closest to the transducer along the propagation path, whereas during rightward propagation it was farthest away. The 15 mm hole showed the opposite relationship. The rectangular groove remained at the same propagation-path distance in the two scan directions. These relationships are consistent with the defect-echo arrival times shown in Figures 13 and 14.

Figure 15 presents the unidirectional-wave B-scan images obtained from the 100 mm diameter pipeline specimen using an EMAT. The probe operated in self-transmit/receive mode. For the left-side scan, coil A led coil B by 90°; for the right-side scan, coil A lagged coil B by 90°. The probe was scanned axially in 1 mm increments. The signal-to-noise ratio of the time-domain waveform was reported as 32.5 dB.

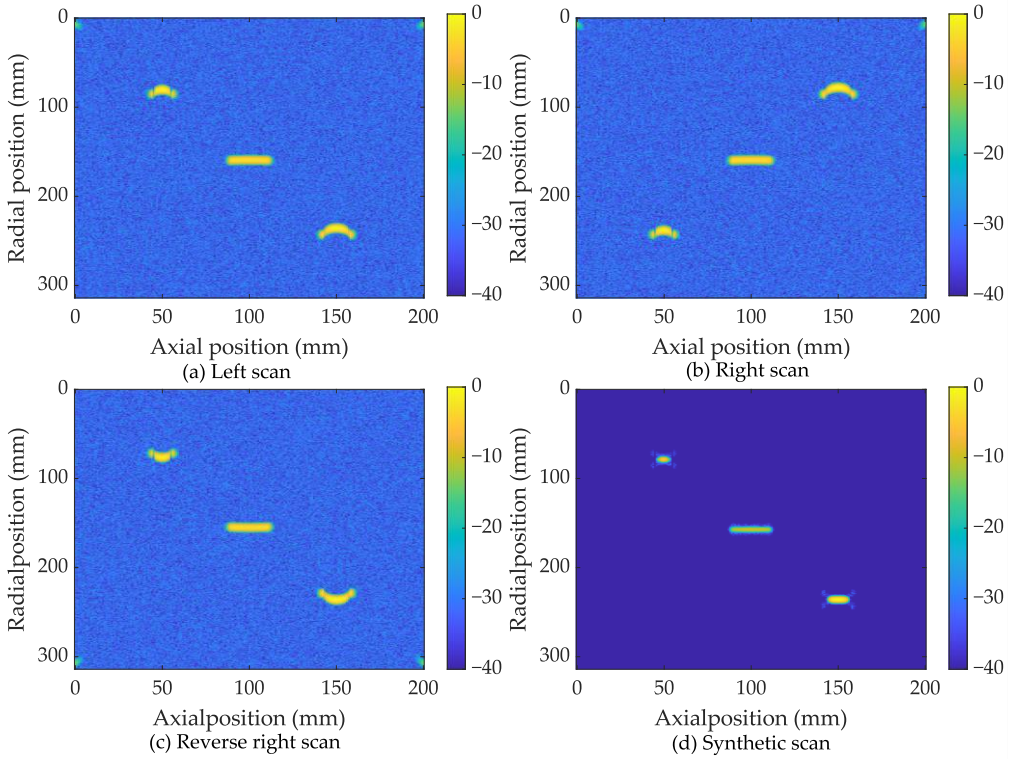


Figure 15. B-scan imaging results of pipeline defects using unidirectional wave.

Each individual B-scan in Figure 15 provides only a partial view of the defects. The left-side scan primarily reveals the leading edge of a defect relative to the propagation direction, whereas the right-side scan primarily reveals the trailing edge. In both images, the reconstructed profiles are distorted, and the defect extent along the propagation direction cannot be reliably determined from either view alone.

To improve reconstruction, the right-side B-scan was first flipped horizontally to align the two scans in a common spatial reference frame. The fused image was then calculated as the Hadamard product of the two B-scan matrices, that is, by multiplying corresponding matrix elements. The synthesized image is shown in Figure 15d. Compared with either individual scan, the fused image represents the defect geometry more completely: both the leading and trailing edges are retained, and the resulting outlines appear more consistent with the nominal defect shapes.

Reconstruction quality depends on the orientation of a defect relative to the wave-propagation direction. The method appears to work more effectively when the defect dimension of interest is perpendicular to the propagation direction, because its leading and trailing boundaries may produce distinct reflections. The rectangular groove, with its 20 mm length oriented perpendicular to the propagation direction, falls into this category and is reconstructed with a relatively clear profile. By comparison, the circular holes are reconstructed less accurately, and their fused profiles appear more elliptical than circular.

The observed distortion may be associated with weaker or more spatially distributed reflections from curved defect boundaries. For a circular hole, the incident wavefront encounters a curved boundary rather than a flat edge, potentially distributing reflected energy over a wider range of directions. Consequently, reflections from the leading and trailing portions of a circular defect may be weaker or less distinct than those from a rectangular groove. In the Hadamard-product fusion, such weak edge responses contribute less strongly, which may lead to a smoothed or elongated reconstructed boundary.

These observations suggest that the proposed bidirectional B-scan synthesis method may be more suitable for defects whose relevant dimension is perpendicular to the wave-propagation direction, such as axial grooves, circumferential cracks, or flat-bottomed holes, subject to the actual orientation and geometry of each defect. For defects aligned parallel to the propagation direction or having curved boundaries, reconstruction accuracy may be limited by weak or diffuse edge reflections.

5. Conclusions

A finite-element model of EMAT-based unidirectional-wave pipeline inspection was developed. The effects of five parameters—magnet width, magnet thickness, coil width, coil thickness, and lift-off distance—were investigated using an orthogonal experimental design to identify a parameter combination for circumferential excitation and reception. Based on the simulation results, EMAT probes and aluminum pipeline specimens containing different defect types were fabricated. An experimental platform was assembled, and imaging tests were conducted. The main conclusions are as follows:

(1) The simulated unidirectional-wave amplitude decreased as the lift-off distance increased and increased gradually with coil width. With increasing magnet width, magnet thickness, and coil thickness, the amplitude first increased and then decreased.

(2) The selected parameter combination was a magnet width of 14 mm, magnet thickness of 8 mm, coil width of 2 mm, coil thickness of 0.2 mm, and lift-off distance of 0.1 mm. Before orthogonal-design optimization, the amplitude was 79.2×10^{-8} mm; the simulated amplitude for the selected combination was 124.6×10^{-8} mm, an increase of approximately 57.3%.

(3) Experimental B-scan results show that the proposed bidirectional B-scan synthesis method, based on unidirectional wave excitation, provides a qualitative visualization and profile assessment of the defects, and is particularly effective for defects whose characteristic dimension is oriented perpendicular to the wave propagation direction.

This study developed and experimentally evaluated a unidirectional-wave excitation method for pipeline EMATs and applied it to defect imaging. The results may inform the design of pipeline EMATs and the selection of excitation parameters for defect inspection. This study also has some limitations: The parameter optimization and imaging validation were conducted using a single aluminum-pipeline geometry, and the two-dimensional simulation does not fully represent three-dimensional circumferential wave propagation. The effects of noise on detection performance, applicability to steel and coated pipelines, and independent validation of wave directionality were not systematically investigated. Future work will address these issues to support further evaluation of unidirectional-wave EMATs for pipeline inspection.

Author Contributions: Conceptualization, Longlong He and Yunlai Zhou; methodology, Longlong He and Yunlai Zhou; software, Longlong He; validation, Longlong He; formal analysis, Longlong He; investigation, Longlong He; resources, Yunlai Zhou.; data curation, Longlong He; writing—original draft preparation, Longlong He; writing—review and editing, Longlong He and Yunlai Zhou; visualization, Longlong He; supervision, Yunlai Zhou.; project administration, Yunlai Zhou; funding acquisition, Yunlai Zhou. All authors have read and agreed to the published version of the manuscript.

Funding: This research received no external funding.

Data Availability Statement: The data that support the findings of this study are available from the author upon reasonable request.

Conflicts of Interest: The authors declare no conflicts of interest.

References

1. Zhang, Y.H.; Qian, Z.H.; Wang, B. Modes Control of Lamb Wave in Plates Using Meander-Line Electromagnetic Acoustic Transducers. *Appl. Sci.* **2020**, *10*, 3491.
2. Park, J.; Moon, J.; Lee, J.; Cho, Y. Nonlinear Ultrasonic-Guided Wave Technique for Microdefect Detection in Steel Wire Rods Using Electromagnetic Acoustic Transducer. *Appl. Sci.* **2020**, *10*, 4479.
3. Wang, S.J.; Liang, Q.; Li, C.; Li, Z.C.; Li, Y.Q. Design of guided wave magnetostrictive patch transducer with vertical static bias magnetic field for pipeline inspection. *Sens. Actuators A Phys.* **2024**, *376*, 115611.
4. Parlak, B.O.; Yavasoglu, H.A. A Comprehensive Analysis of In-Line Inspection Tools and Technologies for Steel Oil and Gas Pipelines. *Sustainability* **2023**, *15*, 2783.
5. Liu, T.H.; Pei, C.X.; Cai, R.; Li, Y.; Chen, Z.M. A flexible and noncontact guided-wave transducer based on coils-only EMAT for pipeline inspection. *Sens. Actuators A Phys.* **2020**, *314*, 112213.
6. Zhang, X.; Li, B.; Zhang, X.L.; Song, X.C.; Tu, J.; Cai, C.; Yuan, J.D.; Wu, Q. Internal and External Pipeline Defect Characterization via High-Frequency Lamb Waves Generated by Unidirectional EMAT. *Sensors* **2023**, *23*, 8843.
7. Lan, Q.S.; Sun, R.T.; Tang, W.B.; Zhang, C.Y.; Liu, Y.; Wang, Y.; Lei, A.; Huang, C.H.; Li, S.L.; Cai, Z.C.; et al. Application of Electromagnetic Ultrasonic Testing Technology in pipeline Defects. *Coatings* **2026**, *16*, 133.
8. Miao, H.C.; Li, F.X. Shear horizontal wave transducers for structural health monitoring and nondestructive testing: A review. *Ultrasonics* **2021**, *114*, 106355.
9. Sun, H.Y.; Peng, L.S.; Huang, S.L.; Wang, Q.; Wang, S.; Zhao, W. Analytical model and optimal focal position selection for oblique point-focusing shear horizontal guided wave EMAT. *Constr. Build. Mater.* **2020**, *258*, 120375.
10. Huang, S.L.; Sun, H.Y.; Shen, G.T.; Wang, B.X.; Wang, Q.; Zou, J.; Wang, S. Characteristics of T(0,1) Guided-Wave Point-Focusing Electromagnetic Acoustic Transducer for Pipeline Inspection. *IEEE Sens. J.* **2020**, *20*, 2895–2903.

11. Liu, Z.H.; Li, A.L.; Wu, B.; He, C.F. Development of a wholly flexible surface wave electromagnetic acoustic transducer for pipeline inspection. *Int. J. Appl. Electromagn. Mech.* **2020**, *62*, 13–29.
12. Fang, Z. A review of non-axisymmetric guided waves and their corresponding transducers for defect detection in circular tube structures. *Smart Mater. Struct.* **2023**, *32*, 063001.
13. Liu, D.R.; Hu, J.T.; Pei, C.X.; Liu, T.H.; Chen, Z.M. Development of a Torsional Guided Wave EMAT for Internal Inspection of Ferromagnetic Pipelines. *IEEE Sens. J.* **2023**, *23*, 26154–26162.
14. Deng, S.; Wang, S.K.; Zhao, B.; Liu, Y.P.; Tan, J.B. Axial stress measurement method for hollow cylindrical steel structures based on non-dispersive characteristics of T (0,1) guided waves. *Measurement* **2023**, *220*, 113332.
15. Xie, C.X.; Liu, T.H.; Pei, C.X.; Jin, Y.; Chen, Z.M. A new longitudinal mode guided-wave EMAT with periodic pulsed electromagnets for non-ferromagnetic pipeline. *Sens. Actuators A Phys.* **2021**, *331*, 112991.
16. Liu, F.L.; Li, J.Y.; Li, Z.Y.; Long, J.; Xu, L.J.; Xie, Y.D. A Novel Noncontact Method for Phase Interface Measurement in Liquid-Filled Pipeline Using Leaky L(0,2) Wave. *IEEE Trans. Instrum. Meas.* **2023**, *72*, 6010710.
17. Wang, C.; Xu, J.; Xiao, W.J.; Wang, L.H. Improvement of PPM EMATs for Detecting Defects in 90° Aluminum Alloy Pipeline Bends. *IEEE Sens. J.* **2024**, *24*, 23684–23693.
18. Hu, Y.; Zhou, J.J.; Yue, W.Y. Research on Crossing-Pipeline Support Structure Defect Detection of EMAT-Excited CSH Wave. *Sensors* **2023**, *23*, 5535.
19. Liu, F.L.; Li, Z.Y.; Huang, X.F.; Ma, L.H.; Li, J.Y.; Pu, H.; Long, J.; Xu, L.J.; Xie, Y.D. A Defects Detection Method of Buried Liquid-Filled Pipelines Based on T(0,1) Guided Waves. *IEEE Trans. Instrum. Meas.* **2024**, *73*, 6003012.
20. Thon, A.; Painchaud-April, G.; Le Duff, A.; Bélanger, P. On the use of a linear array EMAT for remote thickness gauging using the reflected modes on a steel pipeline. *NDT E Int.* **2023**, *139*, 102917.
21. Zhou, J.J.; Li, Y.X.; Zheng, Y.; Wang, Z.H.; Wen, J.B. Development and Experimental Study of an Electromagnetic Ultrasonic Circumferential Guided Wave Transducer That Self-Adapts to the Curvature of High-Temperature Pipeline. *IEEE Sens. J.* **2025**, *25*, 2254–2266.

Disclaimer/Publisher's Note: The statements, opinions and data contained in all publications are solely those of the individual author(s) and contributor(s) and not of MDPI and/or the editor(s). MDPI and/or the editor(s) disclaim responsibility for any injury to people or property resulting from any ideas, methods, instructions or products referred to in the content.

https://doi.org/10.3390/app162110939